**ADVANCED
SCIENCE NEWS**
www.advancedsciencenews.com

**ADVANCED
MATERIALS**
www.advmat.de

COMMUNICATION

Highly Emissive Green Perovskite Nanocrystals in a Solid State Crystalline Matrix

Li Na Quan, Rafael Quintero-Bermudez, Oleksandr Voznyy, Grant Walters, Ankit Jain, James Zhangming Fan, Xueli Zheng, Zhenyu Yang, and Edward H. Sargent*

Perovskite nanocrystals (NCs) have attracted attention due to their high photoluminescence quantum yield (PLQY) in solution; however, maintaining high emission efficiency in the solid state remains a challenge. This study presents a solution-phase synthesis of efficient green-emitting perovskite NCs ($CsPbBr_3$) embedded in robust and air-stable rhombic prism hexabromide (Cs_4PbBr_6) microcrystals, reaching a PLQY of 90%. Theoretical modeling and experimental characterization suggest that lattice matching between the NCs and the matrix contribute to improved passivation, while spatial confinement enhances the radiative rate of the NCs. In addition, dispersing the NCs in a matrix prevents agglomeration, which explains their high PLQY.

It is of urgent importance to solid-state lighting that an efficient green-light emitter (a spectral region known as the "green gap") is found.[1] Development of bright, low-cost, green color converters is therefore an active area of research.[2,3] Metal halide perovskite semiconductors have emerged as a promising material for solution-processed light emitters.[4–10] With an ABX_3 crystal structure—where the A and B cations are bound to an X anion—perovskites offer wide tunability of their bandgap by altering their elemental composition. Furthermore, perovskite nanocrystals (NCs) offer further advantages over their bulk counterparts. In the green spectral region, $CsPbBr_3$ NCs have reached a 90% photoluminescence quantum yield (PLQY) in solution, compared to sub-1% PLQY for bulk $CsPbBr_3$.[11–18]

Translating the high performance of perovskite NCs into solid films is an ongoing area of research.[19,20] $CsPbBr_3$ perovskite NC films have so far only attained a maximum reported PLQY of 18%,[21] indicating that further improvements are required to fill the elusive green gap. One of the main hurdles with perovskite NC films is a decrease in PLQY due to agglomeration of the NCs and subsequent loss of quantum confinement.[21] Polymer encapsulation of NCs has led to moderate improvements, but it remains an unsolved problem to achieve high PLQY in the solid state.[22,23]

Dr. L. N. Quan, R. Quintero-Bermudez, Dr. O. Voznyy,
G. Walters, Dr. A. Jain, J. Z. Fan, X. Zheng, Dr. Z. Yang,
Prof. E. H. Sargent
Department of Electrical and Computer Engineering
University of Toronto
35 St George Street, Toronto, Ontario M5S 1A4, Canada
E-mail: ted.sargent@utoronto.ca

Core–shell structures have evolved as a solution to this problem in conventional nanomaterials, such as II-VI, IV-VI, and III-V quantum dots.[24–26] However, achieving this heterostructuring in halide perovskite NCs has so far proven difficult due to intermixing of halide anions between the core and the shell, leading instead to the formation of mixed-halide perovskite NCs.[12,27]

We hypothesized that passivation by endotaxy, with the same chemical elements but in a different crystal structure, could bypass halide intermixing between the core and the shell. Inspired by the successful fabrication and synthesis of endotaxial systems among two completely different crystal structures,[28–30] we set out to investigate the potential for endotaxy with perovskite NCs. Focusing on $CsPbBr_3$ NCs (green-emitting materials), the ternary phase diagram of Cs, Pb, and Br, shown in **Figure 1**a, were studied. From the ternary phase diagram, both cubic-phase $CsPbBr_3$ perovskite compound and hexagonal-phase Cs_4PbBr_6 fall on the same line connecting the $PbBr_2$ and CsBr precursors.

To determine whether the Cs_4PbBr_6 compound could provide endotaxy to $CsPbBr_3$ NCs, potentially passivating their surfaces, the matching of lattice constants was explored, while allowing the main crystallographic directions of the two materials to rotate and translate freely in space. Computationally it was found that $CsPbBr_3$ NCs can align simultaneously along all three dimensions of the Cs_4PbBr_6 compound lattice (Figure 1b–e and the Supporting Information).

An axis system representing the unit vectors of hexagonal phase Cs_4PbBr_6 (space group: 167) is shown in red in Figure 1b. The intersecting axis system shows the rotation at which the {100} lattice planes of a cubic-phase $CsPbBr_3$ NC aligns with the lattice of Cs_4PbBr_6 (Supporting Information). This match satisfies a $CsPbBr_3$ NC inside a Cs_4PbBr_6 matrix, with enhanced passivation of the surfaces and with practically no strain on the NC. In Figure 1c–e, alignment of a cubic perovskite NC in the matrix is visualized. This alignment between cubic NCs and a geometrically anisotropic hexagonal matrix is of considerable interest. With the intricate crystalline structure of Cs_4PbBr_6, it is unsurprising that Cs_4PbBr_6 lattice spacing could match a multiple of the cubic $CsPbBr_3$ lattice constants; however, it is fortuitous that this lattice matching can be satisfied along all three dimensions simultaneously.

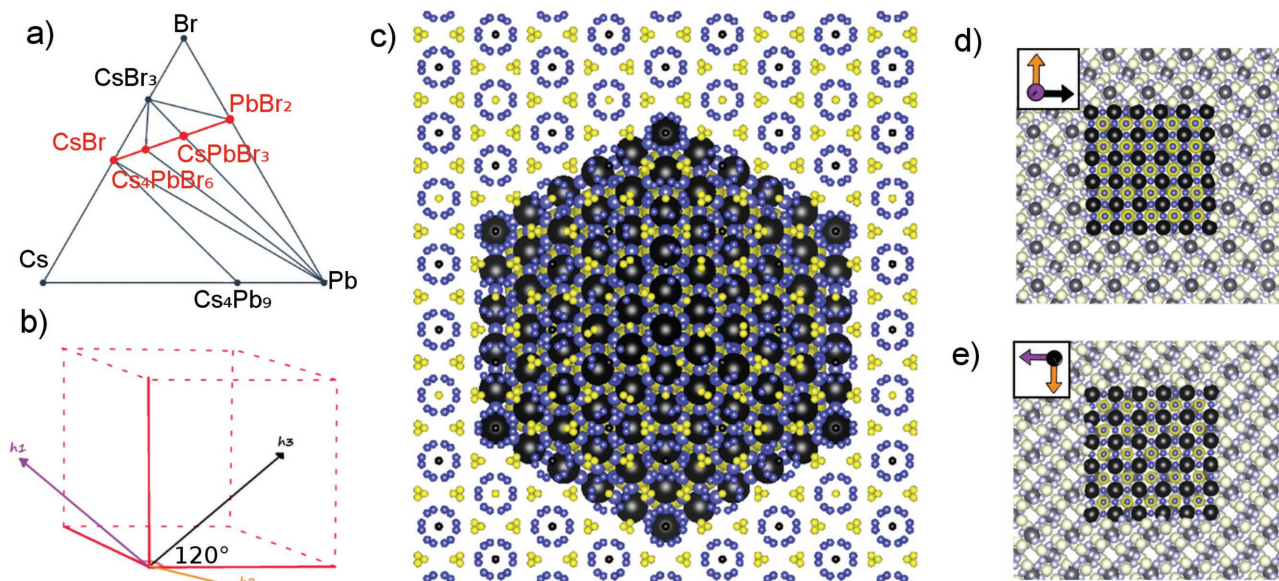The synthesis (Experimental Section and **Figure 2**a) was informed by the ternary phase diagram (Figure 1a). The

Figure 1. Theoretical model of a lattice matched cubic-phase $CsPbBr_3$ perovskite NC in a hexagonal-phase Cs_4PbBr_6 matrix. a) Ternary phase diagram of Cs, Br, and Pb, highlighting the path between precursors CsBr and $PbBr_2$. b) Unit cell of Cs_4PbBr_6 with axes along which cubic perovskite matches with the matrix. c) Cut along the (001) plane of the system, with matrix atoms reduced in size in order to facilitate the observation of the perovskite inclusion in the matrix. d,e) Two different cuts along planes of cubic perovskite (direction-guided arrow colors are consistent with those shown in (b).
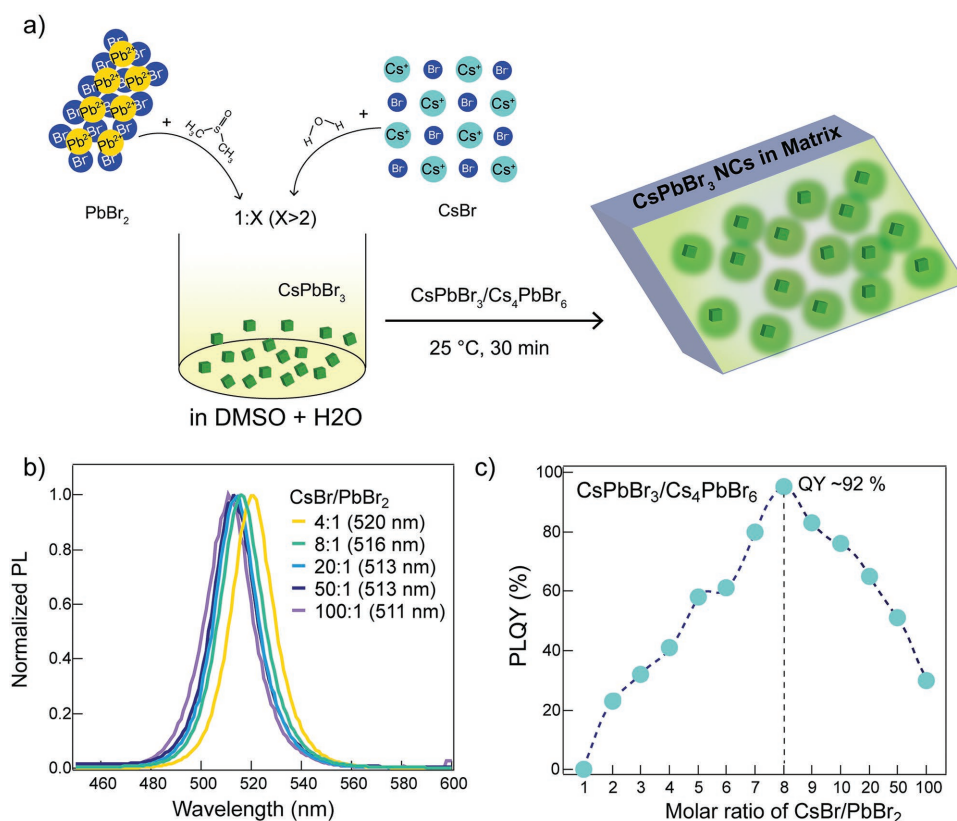

Figure 2. Synthesis of perovskite $CsPbBr_3$-in-Cs_4PbBr_6 microcrystals manifesting high PLQY. a) Graphical representation of the synthesis. b) Photoluminescence emitted and (c) PLQY of materials resulting from different ratios of CsBr and $PbBr_2$.
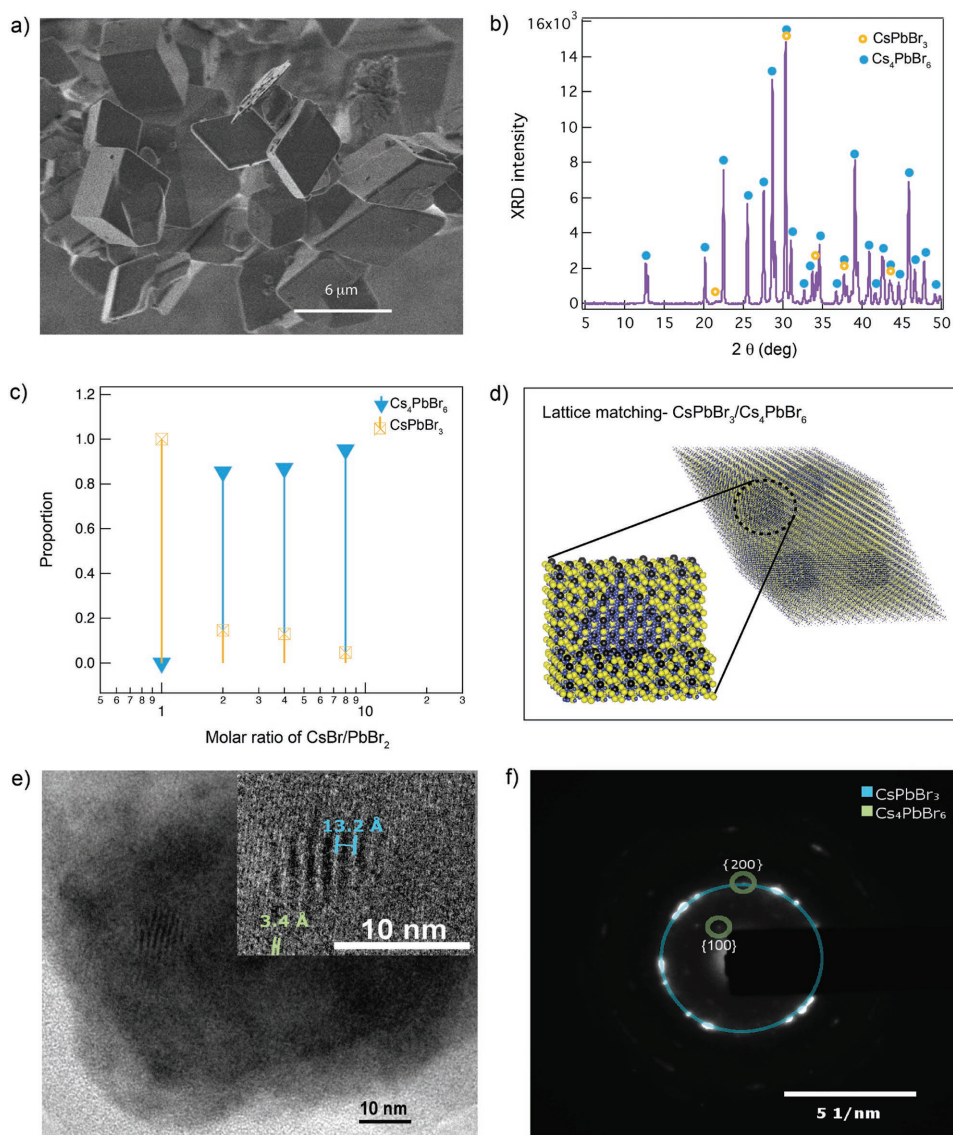
ADVANCED
SCIENCE NEWS
www.advancedsciencenews.com

ADVANCED
MATERIALS
www.advmat.de

COMMUNICATION

Figure 3. Identification and characterization of a hybrid material compound. a) SEM image of the perovskite-in-hexabromide compound. b) XRD spectra of a $CsPbBr_3$-in-Cs_4PbBr_6 crystal. c) Processed ICP-AES data showing the ratio of the compounds. d) Theoretical model for the material with various cubic perovskite inclusions in each rhombic prism matrix. e) High-resolution transmission electron microscopy (HRTEM) image of a $CsPbBr_3$-in-Cs_4PbBr_6 crystal, with an inset showing fast Fourier transform (FFT) of a HRTEM image. f) Selected area electrond diffraction (SAED) pattern of a $CsPbBr_3$-in-Cs_4PbBr_6 crystal, color-coded to identify the compounds. Peaks without color-coding are peaks where both phases overlap.

ternary phase diagram (often called a Gibbs triangle) highlights that various mixtures of the CsBr and $PbBr_2$ precursors can produce different proportions of Cs_4PbBr_6 and $CsPbBr_3$, with no intermediate phases. To overcome the different solubility of $PbBr_2$ and CsBr in polar solvents, aprotic dimethyl sulfoxide (DMSO) solvent was used for dissolving $PbBr_2$, and protic H_2O solvent was used for CsBr. Precise control of the DMSO/H_2O ratio was used to precipitate crystals in the mixed H_2O-DMSO solution, and the precursor ratio was used to control the final product composition. A precursor ratio (CsBr/$PbBr_2$) of 1 leads to $CsPbBr_3$ microcrystals, along with some unused precursors (Figure S5, Supporting Information). As long as the ratio of the precursors was kept above 1, the synthesis resulted in a highly emissive compound (Figure S17, Supporting Information).

A red-shift in photoluminescence (PL) wavelength of the composite material, from 510 to 520 nm, was found as the ratio of CsBr/$PbBr_2$ was increased. This is consistent with the NCs size dependent bandgap; a result of quantum confinement (Figure 2b). The PLQY also varied with precursor concentration (Figures 2c); whereby, the PLQY reached a maximum of 92% at a CsBr/$PbBr_2$ ratio of 8—a significant advance over the previous maximum (61%), which was achieved with polyhedral oligomeric silsesquioxane encapsulation.[22]

Scanning electron microscopy (SEM) images of the resulting microcrystals are shown in **Figure 3**a. The formation of rhombic prisms agrees with Cs_4PbBr_6 compound as a matrix. Powder X-ray diffraction (XRD) (Figure 3b) confirms the coexistence of perovskite and hexabromide compounds

in the material system. Wide area compositional SEM imaging (Figures S2–S4, Supporting Information) and corresponding energy-dispersive X-ray spectroscopy (EDS) mapping (Figures S13–S15, Supporting Information) confirm the presence of a single phase; arguing against the possibility that $CsPbBr_3$ and Cs_4PbBr_6 are present as separate bulk phases. The XRD results indicate more matrix than NCs (i.e., smaller pure-perovskite peaks). An approximate value of the ratio of $CsPbBr_3$ to Cs_4PbBr_6 is determined by measuring the Cs to Pb atomic ratio using inductively coupled plasma atomic emission spectrometry (ICP-AES) (Figure S2, Supporting Information), from which a ratio between $CsPbBr_3$ to Cs_4PbBr_6 is deduced (Figure 3c).

A detailed material structure emerges from aggregate analysis of the PL, SEM, XRD, ICP-AES, and theoretical phase matching between perovskite NCs and Cs_4PbBr_6 (Figure 3d)—rhombic prisms of Cs_4PbBr_6 that contain small cubic $CsPbBr_3$ NCs ($\approx$10 nm dimensions) aligned to the lattice of the matrix. The dimensions of the rhombic prisms range from 4–10 µm. It is possible that micrometric $CsPbBr_3$ impurities are also present in the admixture; however, high PLQY values were measured (which would decrease in the presence of bulk-like $CsPbBr_3$) that were not noticed in SEM imaging (Figures S2–S4, Supporting Information), therefore, it is unlikely that these impurities would considerably affect the measured optical properties. Furthermore, the material shows stable light emission, with very little degradation after a month of storage in air (Figure S18, Supporting Information).

Transmission electron microscopy (TEM), along with SAED, offers the most direct and convincing corroboration of the model in Figure 3d. As TEM could not be used to measure the microcrystal due to its large dimensions, the microcrystal was crushed using a mortar and TEM was performed on thin chips of the crystal. Figure 3e shows a resulting TEM image, where showing a characteristic Cs_4PbBr_6 lattice spacing of 3.4 ± 0.1 Å, and a region with a much larger lattice spacing of 13.2 ± 0.1 Å, representing a Moiré fringe pattern resulting from the beating of two overlapping lattice fringes. Mixing of the measured lattice of the matrix (red) with the lattice of the NC ($\approx$2.94 Å)[31] in the Moiré equation yields a pattern spacing consistent with experimental observations (in blue):

$$d_{Moire} = \frac{d_{NC}^2}{2(d_{Matrix} - d_{NC})} = 10 \pm 3\,\text{Å} \tag{1}$$

The size in the region of interest also matches the dimensions of the expected NC. The SAED results evidence the coexistence of $CsPbBr_3$ and Cs_4PbBr_6 within the microcrystal. The pattern on Figure 3f shows peaks of both phases after an electron beam has diffracted off a single microcrystal chip. The difference in SAED patterns between regions with and without NCs can be identified in Figure S12 (Supporting Information), strongly corroborating the existence of perovskite NCs inside the microcrystals of Cs_4PbBr_6. Further TEM images are included in Figures S10 and S11 (Supporting Information).

A $CsBr/PbBr_2$ precursor ratio of 8 yields microcrystals that exhibit the highest PLQY, due to sufficient spatial separation between their cubic perovskite inclusions, resulting in the best passivation of the NC surface. At lower $CsBr/PbBr_2$ ratios, a decrease in PLQY can be attributed to the growing size of NCs, which is indicated by a red-shift in PL. These larger NCs are bulk-like, therefore exhibiting a loss in quantum confinement and a decrease in PLQY due to higher exciton dissociation. On the other side of the optimum, at small amounts of $PbBr_2$, NC growth is impeded, leading to smaller, nonuniform NCs high in defects (Figure 2b). As the amount of $PbBr_2$ precursor is further reduced (beyond a $CsBr/PbBr_2$ ratio of 20), the microcrystals become smaller, leaving a significant amount of unreacted $CsBr$. At this point, there is very little $CsPbBr_3$ and also little of the passivating Cs_4PbBr_6 matrix.

The wide bandgap matrix allows for direct photoexcitation of the NC inclusions. Photoluminescence excitation (PLE) spectra of NC emission at 515 nm, and matrix emission at 375 nm,[32] are plotted in **Figure 4**a. Notably, there is a sharp dip at $\approx$310 nm, where light is fully absorbed by the matrix and does not reach the NCs. In this region, the Cs_4PbBr_6 matrix exhibits a sharp peak in the absorption spectrum.[33]

PL decay measurements were performed on perovskite NCs in the matrix compound, yielding the traces shown in Figure 4b. Multiexponential functions fit these decay traces, with the values listed in Table S19 (Supporting Information). With similar PL lifetimes to those of colloidal $CsPbBr_3$ perovskite NCs,[13,34,35] transient photophysics further evidences that
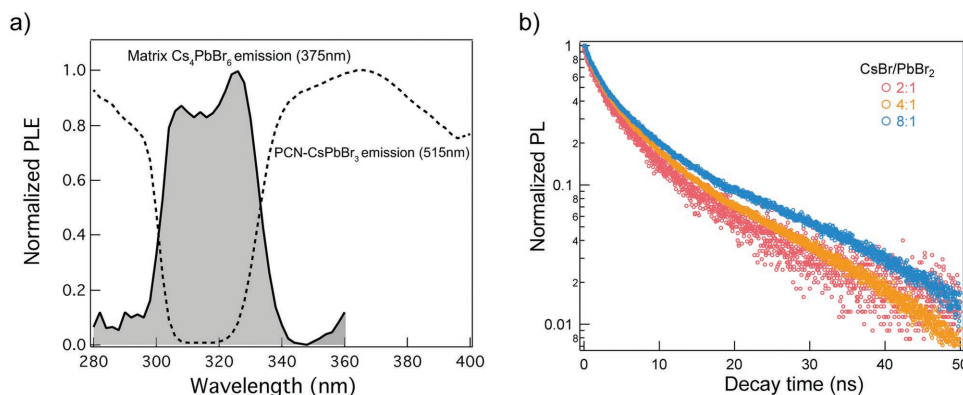

Figure 4. Photophysical behavior of the $CsPbBr_3$-in-Cs_4PbBr_6 material. a) Normalized PLE spectra of the perovskite NCs at 515 nm and the matrix at 375 nm. b) PL decay for crystals with different ratios of CsBr to $PbBr_2$.

these NCs are responsible for the high PLQY emission. The PL lifetimes were further used to compute radiative lifetimes (Table S19, Supporting Information), evidencing an increase in radiative lifetime as the size of the NC is increased, and approaching a maximal value for the bulk-like perovskite microcrystals produced with a $CsBr/PbBr_2$ ratio of 1. This finding agrees with the material model, exhibiting a dramatic increase in radiative lifetime due to an increase in exciton dissociation as the size of a NC is increased into the bulk-like domain.

The synthesis of cubic $CsPbBr_3$ perovskite NCs in robust and air-stable rhombic prism Cs_4PbBr_6 microcrystals enables high emission efficiency in the solid state (92% PLQY). A model informed by experimental characterization and computational evidence of lattice-matching between cubic $CsPbBr_3$ NCs and a Cs_4PbBr_6 matrix is proposed. Powder XRD confirms the coexistence of perovskite NCs and the matrix. SEM imaging and PL confirmed the shape and size of the crystallites. Compound ratios were estimated from ICP-AES measurements. TEM imaging and SAED patterns provide conclusive evidence in support of the material model. Photophysical studies, including PL decay and PLE spectra, corroborated the model. In sum, all of the experimental characterizations agreed with the picture of endotaxy of perovskite NCs with a Cs_4PbBr_6 matrix.

Experimental Section

Synthesis of Bulk Perovskite NCs in Cs_4PbBr_6: 1–0.001 M (depending on the ratio of precursors) of $PbBr_2$ (99.9%, Alfa Aesar) was dissolved in 1 mL DMSO (99.9%, Aldrich). At the same time, 1 M of CsBr (99.999%, Aldrich) was dissolved in 300 µL H_2O (deionized water). $CsBr/H_2O$ solution was then slowly injected into the $PbBr_2$/DMSO solution and stirred at room temperature in air atmosphere for 30 min to 2 h (depending on the concentration of $PbBr_2$). After bright green precipitates formed in the mixed solution, crystals were centrifuged at 5000 rpm and washed with toluene, followed by drying under vacuum.

Fabrication of Film Perovskite NCs in Cs_4PbBr_6: Perovskite NCs in Cs_4PbBr_6 precursor solution were prepared via the same method described above, but the concentration of $PbBr_2$ was fixed to 0.1 M. The series of precursor solution was then spin-coated on the glass substrate, followed by annealing, for atomic force microscopy (AFM) and transient absorption (TA) measurements.

Photoluminescence Measurements (Decay, Emission Spectroscopy, and PLQY): All PL measurements were done with a Horiba Fluorolog time correlated single photon counting system with a single grating spectrometer and photomultiplier tube detector. Steady state PL and PLE measurements were done using monochromatized light from a xenon lamp as the excitation source. Transient measurements used a laser diode ($\lambda = 375$ nm) as the excitation source. The time resolution, according to the instrument response function, is $\Delta t \approx 0.13$ ns. The standard published method for measuring quantum yields[36] was used with a Quanta-Phi integrating sphere. Excitation and emission intensities were measured in empty-sphere, direct illumination, and indirect illumination configurations. Light was coupled between the Fluorolog system and the sphere with optical fiber bundles. The detector and integrating sphere were corrected for spectral variance using a calibrated white light source.

Transient Absorption Spectroscopy: Femtosecond laser pulses of 1030 nm generated by a Yb:KGW laser at a 5 kHz repetition rate (Light Conversion, Pharos) passed through an optical parametric amplifier (Light Conversion, Orpheus) with the second harmonic of the signal pulse selected for 400 nm light. The latter served as the pump pulse, whereas the probe pulse was generated by focusing the initial 1030 nm pulse into a sapphire crystal, resulting in a white-light continuum (Ultrafast, Helios). With a temporal resolution of the system of ≈350 fs, each time step meant delaying the probe pulse with respect to the pump, with time steps increasing exponentially. Every other pump pulse was blocked with a chopper in order to determine the ΔOD. After going through a grating spectrograph, the pulses were measured by means of a charge-coupled device (Ultrafast, Helios). Multiple scans were taken for each sample at each power, and the average of these scans was used. The traces were fitted to the convolution of the instrument response and a sum of the exponential decays.

XRD: The XRD measurements were collected at the MAX Diffraction Facility at McMaster University, using a Bruker Smart6000 CCD area detector with a Bruker 3-circle D8 goniometer, a Rigaku RU200 Cu $K\overline{\alpha}$ rotating anode, and Göebel cross-coupled parallel focusing mirrors. Bisecting angle scans were performed with a 300 s frame exposure, a detector distance of 16.740 cm, and an X-ray beam at 90 mA and 50 kV.

Inductively Coupled Plasma Atomic Emission Spectrometry: The atomic composition of samples was determined using ICP-AES, with the Perkin Elmer Optima 7300DV. 1, 10, 100, 1000 ppm Pb and Cs were used as standards for the calibration. The perovskites in hexabromide samples were dissolved in 10% HCl before ICP-AES characterization.

Supporting Information

Supporting Information is available from the Wiley Online Library or from the author.

[1] J.-L. Liu, J.-L. Zhang, G.-X. Wang, C.-L. Mo, L.-Q. Xu, J. Ding, Z.-J. Quan, X.-L. Wang, S. Pan, C.-D. Zheng, X.-M. Wu, W.-Q. Fang, F.-Y. Jiang, *Chin. Phys. B* **2015**, *24*, 067804.

[2] C. Wetzel, T. Detchprohm, *Proc. SPIE* **2011**, *8123*, 812308.

[3] T. J. Miller, M. A. Haase, X. Sun, B. Hao, J. Zhang, T. L. Smith, T. Ballen, J. Xie, A. S. Barnes, F. Kecman, J. Yang, J. Thielen, C. A. Leatherdale, R. Wirth, A. Biebersdorf, K. Engl, S. Groetsch, *Proc. SPIE – Int. Soc. Opt. Eng.* **2010**, *7617*, 76171A.

[4] H. C. Yoon, H. Kang, S. Lee, J. H. Oh, H. Yang, Y. R. Do, *ACS Appl. Mater. Interfaces* **2016**, *8*, 18189.

[5] S. Pathak, N. Sakai, F. W. R. Rivarola, S. D. Stranks, J. Liu, G. E. Eperon, C. Ducati, K. Wojciechowski, J. T. Griffiths, A. A. Haghighirad, A. Pellaroque, R. H. Friend, H. J. Snaith, *Chem. Mater.* **2015**, *27*, 8066.

[6] J. Wang, N. Wang, Y. Jin, J. Si, Z. K. Tan, H. Du, L. Cheng, X. Dai, S. Bai, H. He, Z. Ye, M. L. Lai, R. H. Friend, W. Huang, *Adv. Mater.* **2015**, *27*, 2311.

[7] H. Cho, S.-H. Jeong, M.-H. Park, Y.-H. Kim, C. Wolf, C.-L. Lee, J. H. Heo, A. Sadhanala, N. Myoung, S. Yoo, S. H. Im, R. H. Friend, T.-W. Lee, *Science* **2015**, *350*, 1222.

COMMUNICATION

[8] M. Saliba, S. M. Wood, J. B. Patel, P. K. Nayak, J. Huang, J. A. Alexander-Webber, B. Wenger, S. D. Stranks, M. T. Hörantner, J. T. W. Wang, R. J. Nicholas, L. M. Herz, M. B. Johnston, S. M. Morris, H. J. Snaith, M. K. Riede, *Adv. Mater.* **2016**, *28*, 923.

[9] B. R. Sutherland, S. Hoogland, M. M. Adachi, C. T. O. Wong, E. H. Sargent, *ACS Nano* **2014**, *8*, 10947.

[10] B. R. Sutherland, E. H. Sargent, *Nat. Photonics* **2016**, *10*, 295.

[11] C. C. Stoumpos, C. D. Malliakas, J. A. Peters, Z. Liu, M. Sebastian, J. Im, T. C. Chasapis, A. C. Wibowo, D. Y. Chung, A. J. Freeman, B. W. Wessels, M. G. Kanatzidis, *Cryst. Growth Des.* **2013**, *13*, 2722.

[12] Q. A. Akkerman, V. D'Innocenzo, S. Accornero, A. Scarpellini, A. Petrozza, M. Prato, L. Manna, *J. Am. Chem. Soc.* **2015**, *137*, 10276.

[13] L. Protesescu, S. Yakunin, M. I. Bodnarchuk, F. Krieg, R. Caputo, C. H. Hendon, R. X. Yang, A. Walsh, M. V. Kovalenko, *Nano Lett.* **2015**, *15*, 3692.

[14] G. Rainò, G. Nedelcu, L. Protesescu, M. I. Bodnarchuk, M. V. Kovalenko, R. F. Mahrt, T. Stöferle, *ACS Nano* **2016**, *10*, 2485.

[15] J. De Roo, M. Ibáñez, P. Geiregat, G. Nedelcu, W. Walravens, J. Maes, J. C. Martins, I. Van Driessche, M. V. Kovalenko, Z. Hens, *ACS Nano* **2016**, *10*, 2071.

[16] A. Swarnkar, R. Chulliyil, V. K. Ravi, M. Irfanullah, A. Chowdhury, A. Nag, *Angew. Chem., Int. Ed.* **2015**, *54*, 15424.

[17] Y. Hassan, Y. Song, R. D. Pensack, A. I. Abdelrahman, Y. Kobayashi, M. A. Winnik, G. D. Scholes, *Adv. Mater.* **2016**, *28*, 566.

[18] S. Bai, Z. Yuan, F. Gao, *J. Mater. Chem. C* **2016**, *4*, 3898.

[19] X. Zhang, H. Lin, H. Huang, C. Reckmeier, Y. Zhang, W. C. H. Choy, A. L. Rogach, *Nano Lett.* **2016**, *16*, 1415.

[20] J. Song, J. Li, X. Li, L. Xu, Y. Dong, H. Zeng, *Adv. Mater.* **2015**, *27*, 7162.

[21] Y. Kim, E. Yassitepe, O. Voznyy, R. Comin, G. Walters, X. Gong, P. Kanjanaboos, A. F. Nogueira, E. H. Sargent, *ACS Appl. Mater. Interfaces* **2015**, *7*, 25007.

[22] H. Huang, B. Chen, Z. Wang, T. F. Hung, A. Susha, H. Zhong, A. Rogach, C. Sci, H. Huang, B. Chen, Z. Wang, T. F. Hung, A. S. Susha, H. Zhong, A. L. Rogach, *Chem. Sci.* **2016**, *7*, 5699.

[23] M. Meyns, M. Perálvarez, A. Heuer-Jungemann, W. Hertog, M. Ibáñez, R. Nafria, A. Genç, J. Arbiol, M. V. Kovalenko, J. Carreras, A. Cabot, A. G. Kanaras, *ACS Appl. Mater. Interfaces* **2016**, *8*, 19579.

[24] E. Ryu, S. Kim, E. Jang, S. Jun, H. Jang, B. Kim, S. W. Kim, *Chem. Mater.* **2009**, *21*, 573.

[25] S. A. Ivanov, A. Piryatinski, J. Nanda, S. Tretiak, K. R. Zavadil, W. O. Wallace, D. Werder, V. I. Klimov, *J. Am. Chem. Soc.* **2007**, *129*, 11708.

[26] G. E. Cragg, A. L. Efros, *Nano Lett.* **2010**, *10*, 313.

[27] G. Nedelcu, L. Protesescu, S. Yakunin, M. I. Bodnarchuk, M. J. Grotevent, M. V. Kovalenko, *Nano Lett.* **2015**, *15*, 5635.

[28] L. D. Zhao, J. He, S. Hao, C. I. Wu, T. P. Hogan, C. Wolverton, V. P. Dravid, M. G. Kanatzidis, *J. Am. Chem. Soc.* **2012**, *134*, 16327.

[29] K. Biswas, J. He, Q. Zhang, G. Wang, C. Uher, V. P. Dravid, M. G. Kanatzidis, *Nat. Chem.* **2011**, *3*, 160.

[30] Z. Ning, X. Gong, R. Comin, G. Walters, F. Fan, O. Voznyy, E. Yassitepe, A. Buin, S. Hoogland, E. H. Sargent, *Nature* **2015**, *523*, 324.

[31] M. Rodová, J. Brožek, *J. Therm. Anal.* **2003**, *71*, 667.

[32] M. Nikl, E. Mihokova, K. Nitsch, F. Somma, C. Giampaolo, G. P. Pazzi, P. Fabeni, S. Zazubovich, *Chem. Phys. Lett.* **1999**, *306*, 280.

[33] S. Kondo, K. Amaya, T. Saito, *J. Phys. Condens. Matter* **2002**, *14*, 2093.

[34] N. S. Makarov, S. Guo, O. Isaienko, W. Liu, I. Robel, V. I. Klimov, *Nano Lett.* **2016**, *16*, 2349.

[35] F. Hu, H. Zhang, C. Sun, C. Yin, B. Lv, C. Zhang, W. W. Yu, X. Wang, Y. Zhang, M. Xiao, *ACS Nano* **2015**, *9*, 12410.

[36] J. C. de Mello, H. F. Wittmannn, R. H. Friend, *Adv. Mater.* **1997**, *9*, 230.